sciendo

TATRA MOUNTAINS
Mathematical Publications

DOI: 10.2478/tmmp-2020-0010
Tatra Mt. Math. Publ. **75** (2020), 147–162

3D CELL IMAGE SEGMENTATION BY MODIFIED SUBJECTIVE SURFACE METHOD

MarKjoe Olunna UBA[1,2] — Karol Mikula[1] — Zuzana Krivá[1] — Hanh Nguyen[3] — Thierry Savy[3] — Eléna Kardash[3] — Nadine Peyriéras [3]

[1]Faculty of Civil Engineering, Slovak University of Technology, Bratislava, SLOVAKIA

[2]Faculty of Physical Sciences, University of Nigeria, Nsukka, NIGERIA

[3]BioEmergences Laboratory (USR 3695), CNRS, University Paris-Saclay, Gif-sur-Yvette, FRANCE

ABSTRACT. In this work, we focused on 3D image segmentation where the segmented surface is reconstructed by the use of 3D digital image information and information from thresholded 3D image in a local neighbourhood. To this end, we applied a mathematical model based on the level set formulation and numerical method which is based on the so-called reduced diamond cell approach. The segmentation approach is based on surface evolution governed by a nonlinear PDE, the modified subjective surface equation. This is done by defining the input to the edge detector function as the weighted sum of norm of presmoothed 3D image and norm of presmoothed thresholded 3D image in a local neighbourhood. For the numerical discretization, we used a semi-implicit finite volume scheme. The method was applied to real data representing 3D microscopy images of cell nuclei within the zebrafish pectoral fin.

1. Introduction

In image processing and computer vision, the goal of image segmentation is to partition the image domain into "meaningful" components. Segmentation

2010 Mathematics Subject Classification: 65M08, 35K61, 68U10.
Keywords: image segmentation, subjective surface method, level set method, finite volume method, semi-implicit scheme, cell microscopy images, zebrafish.
This work has received funding from the European Union's Horizon 2020 research and innovation programme under the Marie Skłodowska-Curie grant agreement no. 721537 and the project APVV-15-0522.
[1]Corresponding author: markjoeuba@gmail.com.

amounts to finding curves in two dimensional (2D) images and computing surfaces in three dimensional (3D) images. It is well known that image segmentation is one of the fundamental and most studied problems in image processing. Consequently, there are several approaches to image segmentation in literature. In this paper, we will focus on the so-called subjective surface segmentation method for image segmentation. In the context of image processing, this method was introduced in [11, 12], studied and applied in several biomedical research [11, 12, 1, 8, 7, 5, 4, 6, 13, 9]. The Subjective surface segmentation method is based on the idea of evolution of segmentation function governed by a geometrical diffusion model. Hence, to segment an object, a segmentation seed (the starting point which determines the approximate position of an object in the image) is usually needed. Then an initial segmentation function $u^0(x)$ is constructed with reference to the segmentation seed. This segmentation function is allowed to evolve to the final state following the subjective surface model. Ideally, the evolution process ends up with a function whose isosurfaces all have the shape of the object that is intended to be segmented. At each time step in the evolution process, we rescale the values of the segmentation function to interval $[0, 1]$. After the last time step in the evolution, we choose the contour 0.5 as the approximate boundary of the object being segmented.

In real applications where the object that is intended to be segmented has internal structures or edges, it is usually difficult to obtain optimal result using the subjective surface segmentation approach. The reason, perhaps, may be due to the fact that this approach works with edge information throughout the segmentation process. Hence, edges within the internal structures in an object of interest are also respected during segmentation. To overcome the effect of the internal structures or edges, we introduced thresholding of values within a ball of appropriate radius around the object center. This local thresholding serves to eliminate the internal structures or edges. Finally, we combined the information gotten from thresholding and original image intensities to get a segmentation result.

2. Mathematical model

Let $I^0 : \Omega \longrightarrow \mathbb{R}$, $\Omega \subset \mathbb{R}^3$ be the intensity function of a 3D image. Let

$$\alpha = \min_{x \in B(c,r)} I^0(x), \qquad \beta = \max_{x \in B(c,r)} I^0(x),$$

where $B(c, r)$ is a ball with radius r centered at c, a given point inside the object to be segmented. Then the threshold value (which is used for local thresholding) may be chosen as $th_r = \lambda\ \alpha + (1 - \lambda)\ \beta$, $\lambda \in [0, 1]$ and the ball radius may be chosen with respect to the approximate size of the object to be segmented.

So, the idea (of local thresholding) is to set all intensity values in the local neighbourhood of center c to β if they are above th_r and α otherwise.

Our method is based on solution of the following modified subjective surface equation

$$u_t = |\nabla u| \nabla \cdot \left(G^0 \frac{\nabla u}{|\nabla u|} \right), \tag{1}$$

where $G^0 = g(\delta |\nabla G_{\sigma_1} * I^0| + \theta |\nabla G_{\sigma_2} * I^{th_r}|)$; u is the unknown segmentation function; $K > 0$ is an empirically chosen parameter [10]; g is the Perona-Malik function typically defined as $g(s) = \frac{1}{1+Ks^2}$; I^{th_r} is 3D image intensity of thresholded image within a ball of radius $r > 0$; $\delta, \theta \in [0, 1]$ determine the influence of information gotten from thresholding and image intensities in the segmentation process; G_{σ_1} and G_{σ_2} are the smoothing kernels. Equation (1) is accompanied by Dirichlet boundary conditions

$$u(t, x) = u^D \ \in [0, T] \times \partial\Omega, \tag{2}$$

and with the initial condition

$$u(0, x) = u^0(x) \ \in \Omega. \tag{3}$$

Without loss of generality, $u^D = 0$ is assumed.

Remark 1. If $\delta = 1$ and $\theta = 0$, then (1) reduces to the subjective surface segmentation model [11].

3. Numerical discretization

3.1. Time discretization

For time discretization of (1), semi-implicit approach which guarantees unconditional stability is used. Suppose that the (1) is solved in time interval $I = [0, T]$ and N equal number of time steps. If $\tau = \frac{T}{N}$ denotes the time step, then the time discretization of (1) is given by

$$\frac{1}{\sqrt{\varepsilon^2 + |\nabla u^{n-1}|^2}} \frac{u^n - u^{n-1}}{\tau} = \nabla \cdot \left(G^0 \frac{\nabla u^n}{\sqrt{\varepsilon^2 + |\nabla u^{n-1}|^2}} \right), \tag{4}$$

where ε is the regularization factor (Evans - Spruck [2]), u^0 is given initial segmentation function, and u^n, $n = 1, \cdots, N$ is the solution of the model in time step n.

3.2. Space discretization

For space discretization, we start with introduction of some notations which will be used subsequently. We have adopted similar notations as those used in [8] and [7]. Let $\mathcal{T}_h$ denote finite volume mesh containing the voxels of 3D image, while V_{ijk}, $i=1,\dots,N_1$, $j=1,\dots,N_2$, $k=1,\dots,N_3$ denote each finite volume. For each $V_{ijk}\in\mathcal{T}_h$, let h_1, h_2, h_3 be the size of the volumes in x_1, x_2, x_3 direction. Let the volume of V_{ijk} and its barycenter be denoted by $m(V_{ijk})$ and c_{ijk}, respectively. Let the approximate value of u^n in c_{ijk} be denoted by u^n_{ijk}. For every $V_{ijk}\in\mathcal{T}_h$, we denote the set of all (p,q,r) such that $p,q,r\in\{-1,0,1\}$, $|p|+|q|+|r|=1$ by N_{ijk}, the set of all (p,q,r), $p,q,r\in\{-1,1\}$ by M_{ijk}, and the set of all (p,q,r) such that $p,q,r\in\{-1,0,1\}$, $|p|+|q|+|r|=2$ by P_{ijk}. For each $(p,q,r)\in N_{ijk}$, denote the line connecting the center of V_{ijk} and the center of its neighbour $V_{i+p,j+q,k+r}$ by σ^{pqr}_{ijk} and its length $m(\sigma^{pqr}_{ijk})$. We denote the planar sides, area and normal of finite volume V_{ijk} by e^{pqr}_{ijk}, $m(e^{pqr}_{ijk})$ and ν^{pqr}_{ijk}, respectively. Let x^{pqr}_{ijk} be the point of intersection between the line σ^{pqr}_{ijk} and planar side e^{pqr}_{ijk}. Furthermore, for each $(p,q,r)\in M_{ijk}$, let s^{pqr}_{ijk} denote the vertices of the finite volume V_{ijk}, and for each $(p,q,r)\in P_{ijk}$, let the midpoints of the voxel edges be denoted y^{pqr}_{ijk}. The approximate value of u^{n-1} in x^{pqr}_{ijk}, y^{pqr}_{ijk} and s^{pqr}_{ijk}, with (p,q,r) belonging to the appropriate index set, is denoted by u^{pqr}_{ijk}; the time index is omitted, as only the values from the time level $n-1$ will be needed at these points.

With these notations, integration of (4) over the finite volume V_{ijk} yields

$$\int\limits_{V_{ijk}}\frac{1}{\sqrt{\varepsilon^2+|\nabla u^{n-1}|^2}}\frac{u^n-u^{n-1}}{\tau}\mathrm{d}x=\int\limits_{V_{ijk}}\nabla\cdot\left(G^0\frac{\nabla u^n}{\sqrt{\varepsilon^2+|\nabla u^{n-1}|^2}}\right)\mathrm{d}x. \tag{5}$$

Let the average value of $A_\varepsilon=\sqrt{\varepsilon^2+|\nabla u^{n-1}|^2}$ in the finite volume V_{ijk} be denoted by $\bar{A}^{n-1}_{\varepsilon,ijk}$. If we consider the fact that u^n and u^{n-1} are asummed to be piecewise constant over the finite volume mesh, then using the divergence theorem we obtain

$$m(V_{ijk})\frac{u^n_{ijk}-u^{n-1}_{ijk}}{\tau}=\bar{A}^{n-1}_{\varepsilon,ijk}\sum_{N_{ijk}}\int\limits_{e^{pqr}_{ijk}}G^0\frac{\nabla u^n}{\sqrt{\varepsilon^2+|\nabla u^{n-1}|^2}}\cdot\nu^{pqr}_{ijk}\mathrm{d}S. \tag{6}$$

If we approximate the normal derivative $\nabla u^n\cdot\nu^{pqr}_{ijk}$ by

$$(u^n_{i+p,j+q,k+r}-u^n_{ijk})/m(\sigma^{pqr}_{ijk})$$

and define $A^{pqr;n-1}_{\varepsilon,ijk}$ and G^{pqr}_{ijk} to be the average of A_ε and G^0 on e^{pqr}_{ijk}, then (6) reduces to

$$m(V_{ijk})\frac{u^n_{ijk}-u^{n-1}_{ijk}}{\tau}=\bar{A}^{n-1}_{\varepsilon,ijk}\sum_{N_{ijk}}m(e^{pqr}_{ijk})G^{pqr}_{ijk}\frac{u^n_{i+p,j+q,k+r}-u^n_{ijk}}{A^{pqr;n-1}_{\varepsilon,ijk}m(\sigma^{pqr}_{ijk})}. \tag{7}$$

Equation (7) can be simplified to

$$u_{ijk}^{n} = u_{ijk}^{n-1} + \frac{\tau}{m(V_{ijk})} \bar{A}_{\varepsilon,ijk}^{n-1} \sum_{N_{ijk}} m(e_{ijk}^{pqr}) G_{ijk}^{pqr} \frac{u_{i+p,j+q,k+r}^{n} - u_{ijk}^{n}}{A_{\varepsilon,ijk}^{pqr;n-1} m(\sigma_{ijk}^{pqr})}, \tag{8}$$

which further simplifies to

$$\left(1 + \frac{\tau}{m(V_{ijk})} \bar{A}_{\varepsilon,ijk}^{n-1} \sum_{N_{ijk}} G_{ijk}^{pqr} \frac{m(e_{ijk}^{pqr})}{A_{\varepsilon,ijk}^{pqr;n-1} m(\sigma_{ijk}^{pqr})}\right) u_{ijk}^{n} -$$

$$\frac{\tau}{m(V_{ijk})} \bar{A}_{\varepsilon,ijk}^{n-1} \sum_{N_{ijk}} G_{ijk}^{pqr} \frac{m(e_{ijk}^{pqr})}{A_{\varepsilon,ijk}^{pqr;n-1} m(\sigma_{ijk}^{pqr})} u_{i+p,j+q,k+r}^{n} = u_{ijk}^{n-1}. \tag{9}$$

Remark 2 (Global rescaling)**.** For each time step n, let

$$\mu = \min_{\Omega} u_{ijk}^{n} \quad \text{and} \quad \xi = \max_{\Omega} u_{ijk}^{n}.$$

Then the rescaled version of u_{ijk}^{n} given by (9) is obtained by the following relation $u_{ijk}^{n} = \frac{1}{\xi - \mu}(u_{ijk}^{n} - \mu)$. Consequently, we have that for each time step n, rescaled version $u_{ijk}^{n} \in [0, 1]$ and it is used in the next time step.

Equation (9) accompanied by the zero Dirichlet boundary condition represents a linear system of equations which can be solved efficiently by the Successive Overrelaxation (SOR) method. Finally, the average values G_{ijk}^{pqr}, $A_{\varepsilon,ijk}^{pqr;n-1}$ and $\bar{A}_{\varepsilon,ijk}^{n-1}$ either in voxels or on voxel sides can be determined. To determine these quantities, the reduced diamond cell strategy (see [7]) was used. The idea of the reduced diamond cell approach is to do away with the values in the eight corner points denoted by $c_{i,j+q,k+r}$, $c_{i+1,j+q,k+r}$, with $q, r \in \{-1, 1\}$ and consequently reducing the stencil from 18 to 10 points. Hence, from the computational point of view, this approach reduces the computational cost.

Furthermore, in the light of this reduced diamond approach, the values of u^{n-1} are obtained from the midpoints y_{ijk}^{pqr} of the voxel edges. These values are approximated for each $(p, q, r) \in P_{ijk}$ by

$$\begin{aligned}
u_{ijk}^{pq0} &= \frac{1}{4}\Big(u_{ijk}^{n-1} + u_{i+p,j,k}^{n-1} + u_{i,j+q,k}^{n-1} + u_{i+p,j+q,k}^{n-1}\Big), \\
u_{ijk}^{p0r} &= \frac{1}{4}\Big(u_{ijk}^{n-1} + u_{i+p,j,k}^{n-1} + u_{i,j,k+r}^{n-1} + u_{i+p,j,k+r}^{n-1}\Big), \\
u_{ijk}^{0qr} &= \frac{1}{4}\Big(u_{ijk}^{n-1} + u_{i,j+q,k}^{n-1} + u_{i,j,k+r}^{n-1} + u_{i,j+q,k+r}^{n-1}\Big).
\end{aligned}$$

For the components of the averaged gradient on e_{ijk}^{pqr}, they are approximated by 2D diamond cell approach in othorgonal planes which use the values u_{ijk}^{pqr} given above (see also [7]). This implies that

$$\nabla^{p00}u_{ijk}^{n-1} = \frac{1}{m(e_{ijk}^{p00})}\int\limits_{e_{ijk}^{p00}} \nabla u^{n-1}\mathrm{d}x \tag{10}$$

$$\approx \left(p\Big(u_{i+p,j,k}^{n-1}-u_{ijk}^{n-1}\Big)/h_1, \Big(u_{ijk}^{p,1,0}-u_{ijk}^{p,-1,0}\Big)/h_2, \Big(u_{ijk}^{p,0,1}-u_{ijk}^{p,0,-1}\Big)/h_3\right),$$

$$\nabla^{0q0}u_{ijk}^{n-1} = \frac{1}{m(e_{ijk}^{0q0})}\int\limits_{e_{ijk}^{0q0}} \nabla u^{n-1}\mathrm{d}x \tag{11}$$

$$\approx \left(\Big(u_{ijk}^{1,q,0}-u_{ijk}^{-1,q,0}\Big)/h_1, q\Big(u_{i,j+q,k}^{n-1}-u_{ijk}^{n-1}\Big)/h_2, \Big(u_{ijk}^{0,q,1}-u_{ijk}^{0,q,-1}\Big)/h_3\right),$$

$$\nabla^{00r}u_{ijk}^{n-1} = \frac{1}{m(e_{ijk}^{00r})}\int\limits_{e_{ijk}^{00r}} \nabla u^{n-1}\mathrm{d}x \tag{12}$$

$$\approx \left(\Big(u_{ijk}^{1,0,r}-u_{ijk}^{-1,0,r}\Big)/h_1, \Big(u_{ijk}^{0,1,r}-u_{ijk}^{0,-1,r}\Big)/h_2, r\Big(u_{i,j,k+r}^{n-1}-u_{ijk}^{n-1}\Big)/h_3\right).$$

Hence, we obtain the approximations $\nabla^{pqr}u_{ijk}^{n-1}$ for the gradient at the points x_{ijk}^{pqr}. Here, the approximation of the gradient in the barycenters x_{ijk}^{pqr} of voxel side e_{ijk}^{pqr} has been denoted by $\nabla^{pqr}u_{ijk}^{n-1}$. If the same approach for computation of gradients of image intensities is used, then the following required approximations are obtained as

$$G_{ijk}^{pqr} = g\Big(\delta|\nabla^{pqr}I_{\sigma_1;ijk}| + \theta|\nabla^{pqr}I_{\sigma_2;ijk}^{th_r}|\Big), \tag{13}$$

$$A_{\varepsilon,ijk}^{pqr;n-1} = \sqrt{\varepsilon^2 + |\nabla^{pqr}u_{ijk}^{n-1}|^2},$$

$$\bar{A}_{\varepsilon,ijk}^{n-1} = \sqrt{\varepsilon^2 + \frac{1}{6}\sum_{N_{ijk}} |\nabla^{pqr}u_{ijk}^{n-1}|^2}.$$

4. Numerical experiments

In this section, several experiments were performed on biological data of the developing pectoral fin in zebrafish embryo to demonstrate the performance of our mathematical model (1). In all the experiments, isosurface 0.5 was displayed. 3D microscopy images of cell nuclei in the pectoral fin were provided

by the group of Nadine Peyriéras, (CNRS BioEmergences, France, in the framework of ImageInLife EC funded project). Pectoral fin in zebrafish serves as a vertebrate model for limb development. To understand how 3D fin shape emerges during growth, it is important to follow cellular rearrangements in this process. Individual cells are detected by labeling their nuclei and observing them under the fluorescence microscope. The nuclei shapes are extracted during segmentation step. Due to the high density of cells in the fin tissue, manual segmentation is time-consuming, laborious and error-prone. Therefore, it is necessary to improve the classical subjective surface algorithm to produce accurate results comparable to manual segmentation. The 3D datasets of the cell nuclei in the pectoral fin in live zebrafish embryos at about 30 hours post fertilization were acquired on an upright confocal microscope Zeiss LSM 780 at the xy resolution of 0.55351075μm/pixel and 1.25μm/pixel z-direction. To label cell nuclei, the wild type embryos were injected with mRNA encoding NLS-EosFP at one-cell stage. The cell centers were obtained using Difference of Gaussians algorithms and further validated using the software Mov-IT implemented in the BioEmergences Workflow [3].

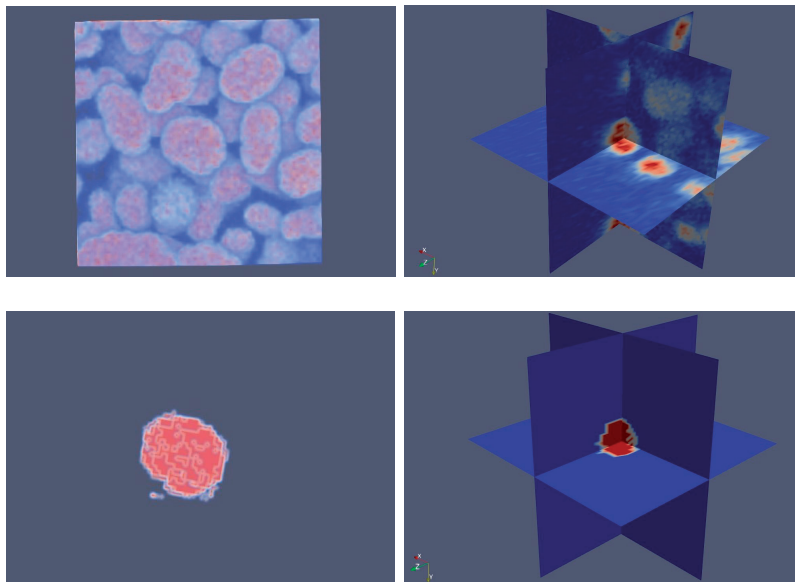

FIGURE 1. The first column of this figure shows the 3D volume rendering of the original 3D image intensity (up) and the 3D image intensity after local thresholding (down), while the second column shows their 2D slices along x, y and z axes.

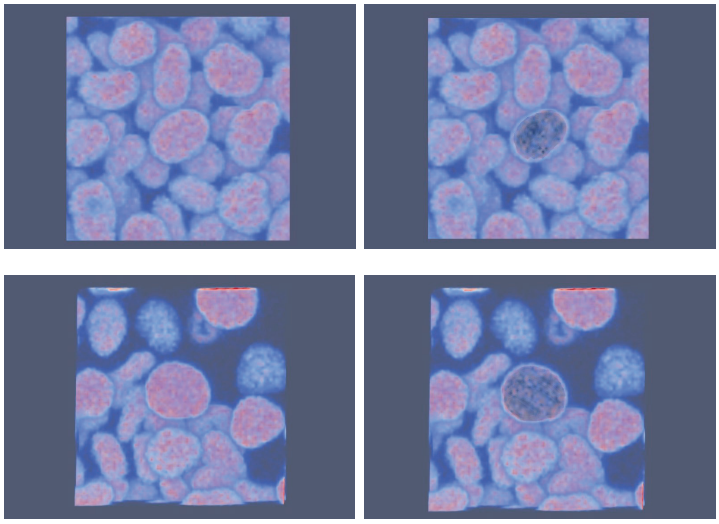

FIGURE 2. The first column of this figure shows the 3D volume rendering of the 3D image which is intended to be segmented, while the second column shows the result after application of (1) with $\delta = 1.0$ and $\theta = 0.0$.

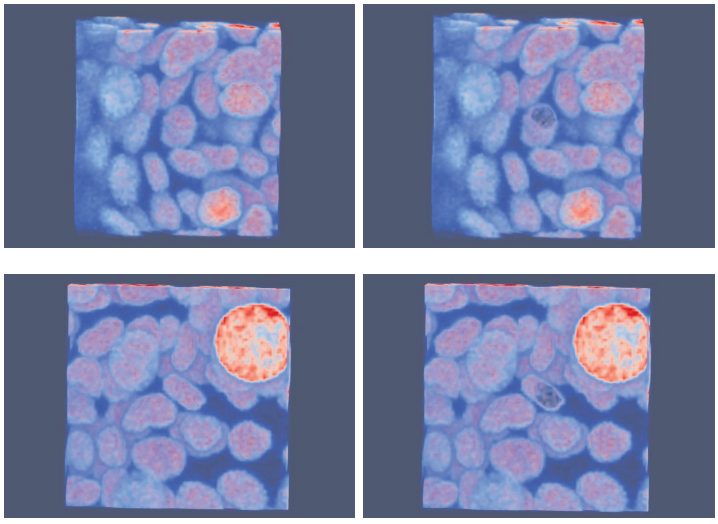

FIGURE 3. The first column of this figure shows the 3D volume rendering of the 3D image which is intended to be segmented, while the second column shows the result after application of (1) with $\delta = 1.0$ and $\theta = 0.0$. In each column, the cell nuclei of interest is located approximately at the center of each picture.

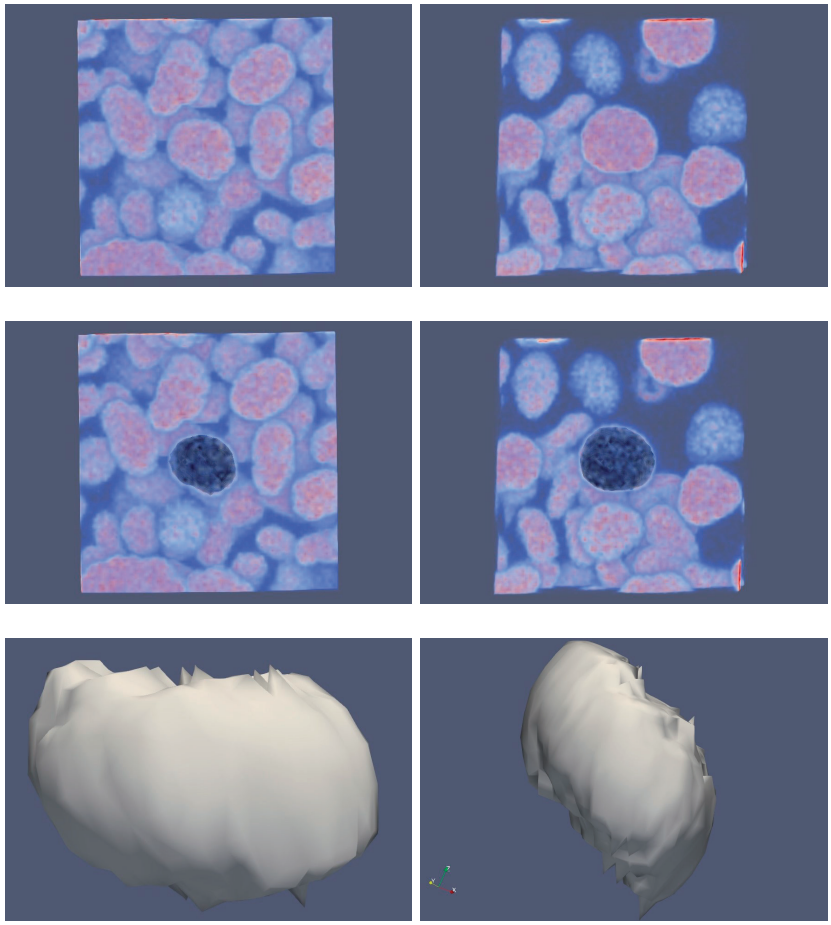

FIGURE 4. The first column shows the 3D volume rendering of a cell nucleus, its reconstruction using $\delta = 0.0$ and $\theta = 1.0$ in (1) and 0.5 isosurface. The second column shows the 3D volume rendering of another cell nucleus, its reconstruction using $\delta = 0.0$ and $\theta = 1.0$ in (1) and 0.5 isosurface.

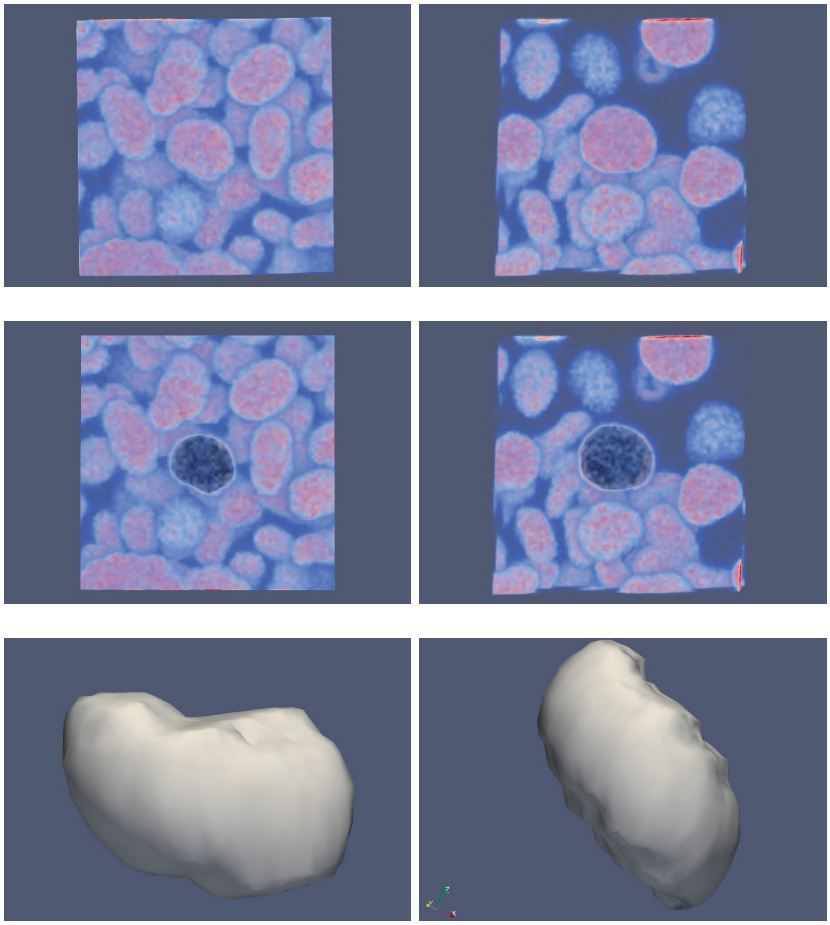

FIGURE 5. The first column shows the 3D volume rendering of a cell nucleus, its reconstruction using $\delta = 0.5$ and $\theta = 0.5$ in (1) and 0.5 isosurface. The second column shows the 3D volume rendering of another cell nucleus, its reconstruction using $\delta = 0.5$ and $\theta = 0.5$ in (1) and 0.5 isosurface.

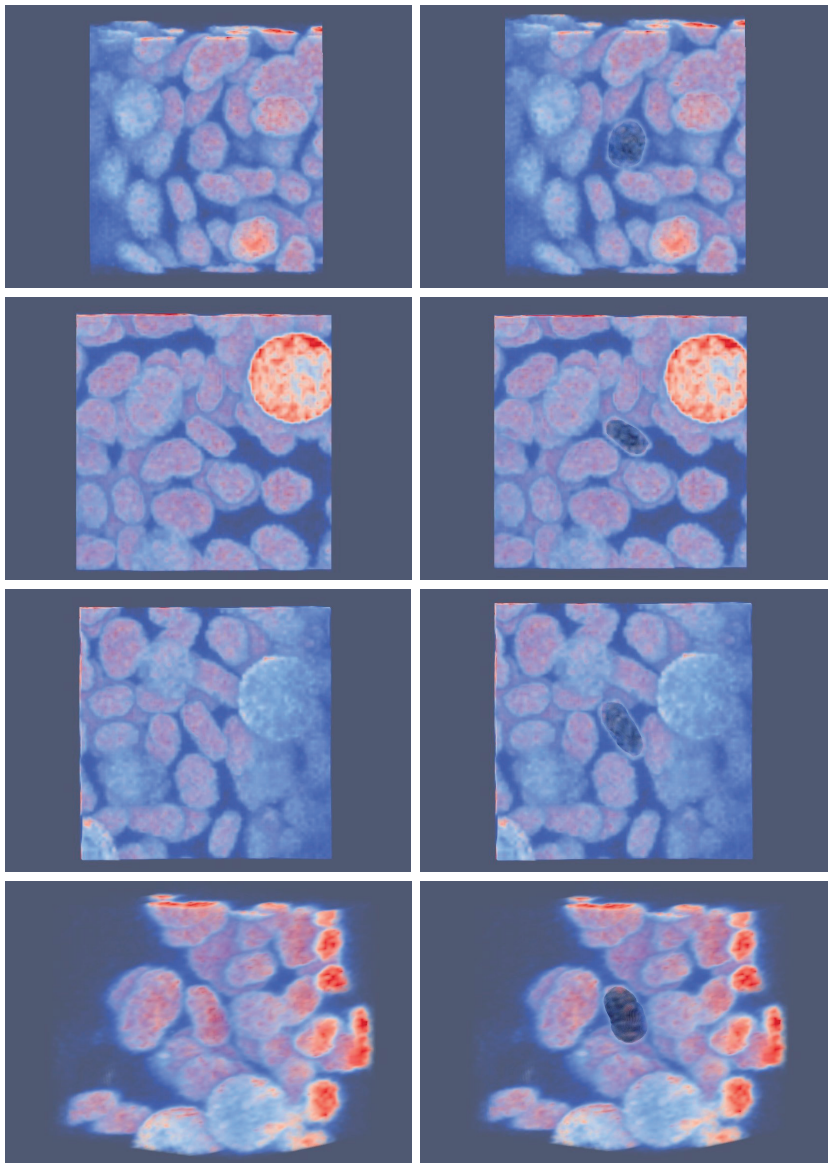

FIGURE 6. In this figure, the first column shows the 3D volume rendering of four different cells nuclei; the second column shows segmentation result using thresholded image intensity information and original image intensity information in (1). That is, the result after application of (1) with $\delta = 0.5$ and $\theta = 0.5$. In each column, the cell nuclei of interest is located approximately at the center of each picture.

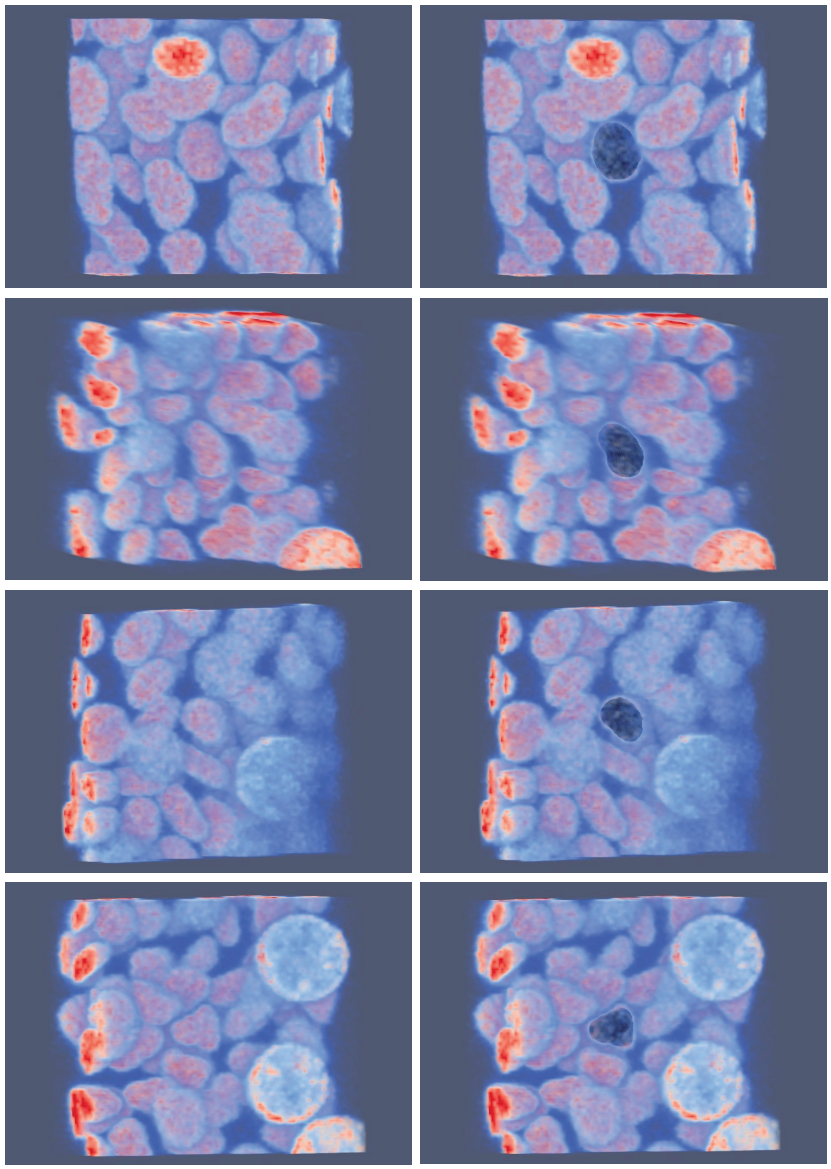

FIGURE 7. The first column shows the 3D volume rendering of four different cells nuclei whereas the second column shows segmentation result using thresholded image intensity information and original image intensity information, that is using $\delta = 0.5$ and $\theta = 0.5$, in (1). In each column, the cell nuclei of interest is located approximately at the center of each picture.

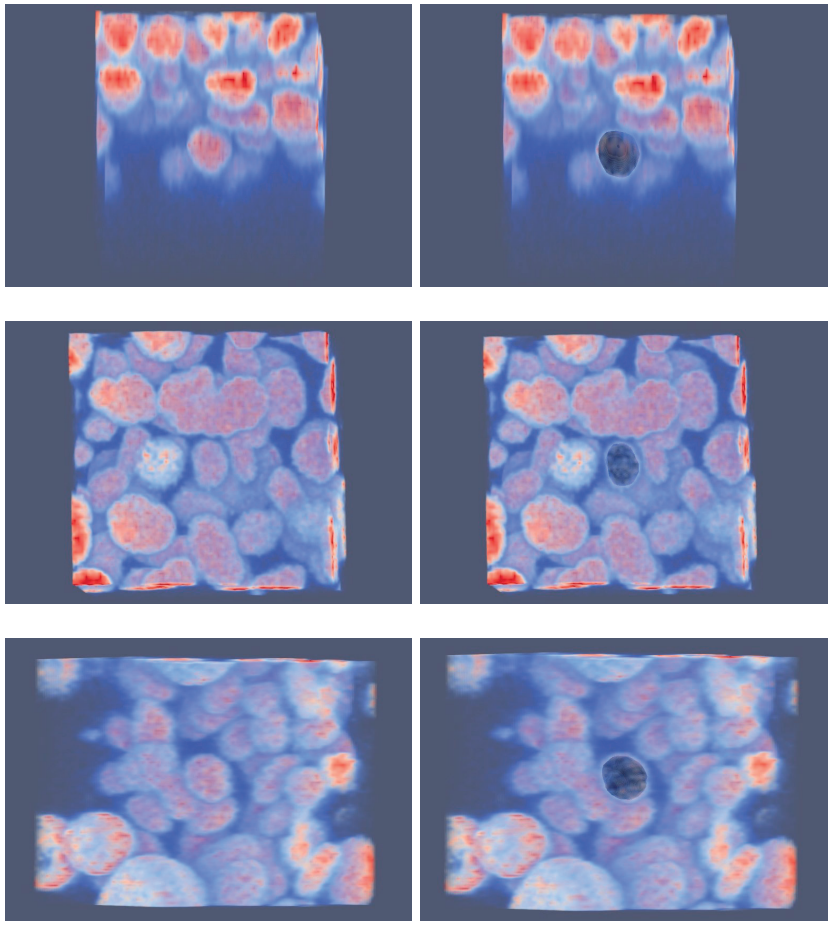

FIGURE 8. In this figure, the first column shows the 3D volume rendering of three different cells nuclei while the second column shows segmentation result using thresholded image intensity information and original image intensity information, that is using $\delta = 0.5$ and $\theta = 0.5$, in (1). In each column, the cell nuclei of interest is located approximately at the center of each picture.

Remark 3. Figure 1 shows the original 3D image intensity and the result of local thresholding. In the first column of this figure, the first row shows the 3D volume rendering of the original 3D image intensity while the second row shows the 3D volume rendering of 3D image intensity after local thresholding. The second column shows their 2D slices along x, y and z axes.

Remark 4. In all Figures 2−8, the first column shows the 3D volume rendering of the original 3D image intensity and the second column shows, in black colour, their corresponding results after segmentation.

Remark 5. In Figures 1−8, the cell nuclei of interest and their corresponding results after segmentation (which are depicted in black colour) are located approximately at the center of each picture.

For the first numerical experiment, $\delta = 1.0$ and $\theta = 0.0$ were used. This choice of parameters reduced equation (1) to the classical subjective surface model [11]. Some good segmentation results were obtained, see e.g. Figure 2. However, several results obtained using these parameters were not optimal, see, for example, Figure 3.

In the second experiment, $\delta = 0.0$ and $\theta = 1.0$ were used. The results obtained, as can be seen from second row of Figure 4, were good. Nevertheless, the problem with this choice of parameters is that the reconstructed surface is not smooth. This can be seen in the last row of Figure 4. Moreover, it can be seen from Figure 5 that the result obtained after applying model (1) is very similar to the one shown in Figure 4 and the isosurface representing the reconstructed surface is smooth.

Finally, several examples of 3D image segmentation involving the us of model (1) with $\delta = 0.5$ and $\theta = 0.5$ were performed. Results of these numerical experiments are shown in Figures 5, 6, 7 and 8. In conclusion, it is easy to see that mathematical model (1) is a useful and successful generalization of the classical subjective surface model.

Remark 6. In these numerical experiments, calculations were executed on a grid with $72 \times 72 \times 32$ voxels, and computational method parameters were set to

$$\begin{array}{lllllllll} h & = & 0.01\,, & \tau & = & 0.1\,, & \lambda & = & 0.7\,, \\ r & = & 12\,, & K & = & 5\,, & N & = & 100\,. \end{array}$$

Acknowledgements. This work has received funding from the European Union's Horizon 2020 research and innovation programme under the Marie Skłodowska-Curie grant agreement no. 721537 and the project APVV-15-0522.

REFERENCES

[1] CORSARO, S.—MIKULA, K.—SARTI, A.—SGALLARI, F.: *Semi-implicit co-volume method in 3D image segmentation*, SIAM J. Sci. Comput. **28** (2006), no. 6, 2248–2265.

[2] EVANS, L. C.—SPRUCK, J.: , *Motion of level sets by mean curvature I*, J. Differential Geom. **33** (1991), 635–681. DOI:10.4310/jdg/1214446559

[3] FAURE, E.—SAVY, T.—RIZZI, B.—MELANI, C.—DRBLÍKOVÁ, O.—FABREGÈS, D.—ŠPIR, R.—HAMMONS, M.—ČUNDERLÍK, R.—RECHER, G.—LOMBARDOT, B.—DULOQUIN, L.—COLIN, I.—KOLLÁR, J.—DESNOULEZ, S.—AFFATICATI, P.—MAURY, B.—BOYREAU, A.—NIEF, J.—CALVAT, P.—VERNIER, P.—FRAIN, M.—LUTFALLA, G.—KERGOSIEN, Y.—SURET, P.—REMEŠÍKOVÁ, M.—DOURSAT, R.—SARTI, A.—MIKULA, K.—PEYRIÉRAS, N.— BOURGINE, P.: *An algorithmic workflow for the automated processing of 3D+time microscopy imaging of developing organisms and reconstruction of their cell lineage*, Nature Commun. **7** (2016), February 2016. Article number: 8674, DOI:10.1038/ncomms9674, `https://www.math.sk/mikula/NCOMMS-15-07907-T_MainArticle.pdf`

[4] FROLKOVIČ, P.—MIKULA, K.—PEYRIÉRAS, N.—SARTI, A.: *A counting number of cells and cell segmentation using advection-diffusion equations*, Kybernetika, **43** (2007), no. 6, 817–829.

[5] KÓSA, B.—MIKULA, K.—UBA, M. O.—WEBERLING, A.—CHRISTODOULOU, N.—ZERNICKA-GOETZ, M.: *3D Image Segmentation Supported by A Point Cloud*, Discrete and Continuous Dynamical Systems - Series S (DCDS-S), (Submitted).

[6] MIKULA, K.—SARTI, A.—SGALLARI, F.: *Co-volume level set method in subjective surface based medical image segmentation*. In: *Handbook of Medical Image Analysis: Segmentation and Registration Models* (J. Suri et al., eds.), Springer, New York, 2005, pp. 583–626.

[7] MIKULA, K.—REMEŠÍKOVÁ, M.: *Finite volume schemes for the generalized subjective surface equation in image segmentation*, Kybernetika **4**, no. 4 (2009), 646–656.

[8] MIKULA, K.—PEYRIÉRAS, N.—REMEŠÍKOVÁ, M.—SARTI, A.: *3D embryogenesis image segmentation by the generalized subjective surface method using the finite volume technique*. In: *Finite Volumes for Complex Applications V: Problems and Perspectives* (R. Eymard, J. M. Herard, eds.), ISTE and WILEY, London, 2008, pp. 585–592.

[9] MIKULA, K.—PEYRIÉRAS, N.—REMEŠÍKOVÁ, M.—STAŠOVÁ, O.: *Segmentation and analysis of 3D zebrafish cell image data*. In: *Proc. of the 3rd International Congress on Image and Signal Processing CISP-BMEI 2010, Yantai, China*, Vol. 3 (2010), pp. 1444–1448.

[10] PERONA, P.—MALIK, J.: , *Scale-space and edge detection using anisotropic diffusion, IEEE Transactions on Pattern Analysis and Machine Intelligence* **12** (1990), 629–639. DOI:10.1109/34.56205

[11] SARTI, A.—MALLADI, R.—SETHIAN, J. A.: *Subjective surfaces: a method for completing missing boundaries*. In: *Proc. Natl. Acad. Sci. USA 97* (2000), no. 12, pp. 6258–6263.

[12] SARTI, A.—MALLADI, R.—SETHIAN, J. A.: , *Subjective Surfaces: a geometric model for boundary completion*, Int. J. Comput. Vis. **46** (2002), no. 3, 201–221.

[13] ZANELLA, C.—RIZZI, B.—MELANI, C.—CAMPANA, M.—BOURGINE, P.—MIKULA, K.—PEYRIÉRAS, N.—SARTI, A.: *Segmentation of cells from 3-d confocal images of live zebrafish embryo*. In: *Conf. Proc. IEEE Eng. Med. Biol. Soc. 2007* (2007), 6027–30.

Received May 16, 2019

MarKjoe Olunna UBA
Karol Mikula
Zuzana Krivá
Department of Mathematics and
Descriptive Geometry
Faculty of Civil Engineering
Slovak University of Technology
Radlinského 11
810 05 Bratislava
SLOVAKIA

E-mail: markjoe.uba@stuba.sk
karol.mikula@gmail.com
kriva@math.sk

MarKjoe Olunna UBA
Department of Mathematics
Faculty of Physical Sciences
University of Nigeria
410001 Nsukka
NIGERIA

E-mail: markjoe.uba@unn.edu.ng
markjoeuba@gmail.com

Hanh Nguyen
Thierry Savy
Eléna Kardash
Nadine Peyriéras
BioEmergences Laboratory
(USR 3695), CNRS
University Paris-Saclay
91190, Gif-sur-Yvette
FRANCE

E-mail: thi.ngoc.hanh.nguyen@cnrs.fr
thierry.savy@gmail.com
elena.kardash@cnrs.fr
nadine.peyrieras@inaf.cnrs-gif.fr